Chemical ordering and magnetism in face-centered cubic CrCoNi alloy

SHEULY GHOSH

s.ghosh@mpie.de

Max-Planck-Institut für Eisenforschung GmbH

Katharina Ueltzen

Federal Institute for Materials Research and Testing https://orcid.org/0009-0003-2967-1182

Janine George

Bundesanstalt für Materialforschung und -prüfung https://orcid.org/0000-0001-8907-0336

Jörg Neugebauer

Max-Planck-Institut für Eisenforschung https://orcid.org/0000-0002-7903-2472

Fritz Körmann

Max-Planck-Institut für Eisenforschung GmbH

Article

Keywords:

Posted Date: March 22nd, 2024

DOI: https://doi.org/10.21203/rs.3.rs-3978660/v1

Additional Declarations:
(Not answered)

Competing interests: The authors declare no competing interests.

Chemical ordering and magnetism in face-centered cubic CrCoNi alloy

Sheuly Ghosh,[1,*] Katharina Ueltzen,[2] Janine George,[2,3] Jörg Neugebauer,[1] and Fritz Körmann[1,2,4,5]

[1] *Computational Materials Design, Max-Planck-Institut für Eisenforschung GmbH, D-40237 Düsseldorf, Germany*
[2] *Federal Institute for Materials Research and Testing Department Materials Chemistry, Unter den Eichen 87, 12205 Berlin*
[3] *Friedrich-Schiller-Universität Jena, Institute of Condensed Matter Theory and Optics, Max-Wien-Platz 1, 07743 Jena*
[4] *Institute for Materials Science, University of Stuttgart, Pfaffenwaldring 55, 70569 Stuttgart, Germany*
[5] *Interdisciplinary Centre for Advanced Materials Simulation (ICAMS), Ruhr-Universität Bochum, 44801, Germany*

(Dated: February 21, 2024)

The impact of magnetism on chemical ordering in face-centered cubic CrCoNi medium entropy alloy is studied by a combination of *ab initio* simulations, machine learning potentials, and Monte Carlo simulations. Large magnetic energies are revealed for some mixed $L1_2/L1_0$ type ordered configurations, which are rooted in strong nearest-neighbor magnetic exchange interactions and chemical bonding among the constituent elements. There is a delicate interplay between magnetism and stability of $MoPt_2$ and $L1_2/L1_0$ type of ordering which may explain opposing experimental and theoretical findings.

I. INTRODUCTION

The role of chemical short-range ordering (SRO) in multi-component alloys such as high and medium entropy alloys, has received substantial attention in recent years [1–21]. While from a thermodynamic-statistical point of view, in the presence of non-vanishing interatomic interactions, SRO always appears to some extent, its quantification and possible impact on material properties is hardly tractable and often unknown. In particular face-centered cubic CrCoNi, a prototypical multi-component alloy combining the challenges of magnetism and chemical complexity, is currently being subject of numerous experimental and theoretical efforts to quantify SRO and its possible implications[8, 22–35]. This alloy's emergence as a material of interest is due to its remarkable mechanical properties, including high tensile strength, ductility, exceptional fracture toughness, irradiation resistance, and quantum critical behavior at low temperatures[36–41].

While initial experimental phase diagram determinations suggested a solid solution face-centered cubic (FCC) phase[42–44], these reports lacked atomistic ordering details. Tamm *et al.* first theoretically examined chemical ordering in CrCoNi using density-functional theory (DFT) energy-based lattice Monte Carlo simulations[23]. They found a trend of increased Cr-Co and Cr-Ni neighbors at the expense of Cr–Cr pairs. The qualitative trend was subsequently corroborated experimentally through local structure analysis by Zhang *et al.*, employing x-ray and neutron total scattering and extended x-ray absorption fine structure (EXAFS) techniques[24]. Ding *et al.*[25] computational study also aligned with Tamm *et al.* predicted ordering tendencies. Though the ordering tendencies were suggested, the actual atomic ordering was not reported. A first possible ground state ordering has been suggested by Pei *et al.* based on Monte Carlo simulations utilizing the cluster expansion technique fitted to DFT [27]. The authors proposed an ordering on the FCC lattice with an alternating pattern of one Cr atomic layer and two mixed Co/Ni atomic layers in the (100) direction[27]. Using a combination of DFT and on-lattice machine learning potentials with subsequent canonical Monte Carlo simulations, an energetically much more preferable $MoPt_2$-like ordering has been revealed by Ghosh *et al.*[31], characterized by a similar alternation of one layer of Cr atoms and two layers of mixed Co and Ni atoms, but in the (110) direction. This $MoPt_2$-type arrangement, noteworthy also found in Cr-Ni binary alloys, has also been reported by Du *et al.*[45] employing a DFT-based neural network potential in hybrid Monte Carlo/molecular dynamics simulations. They also suggested the presence of local $L1_0$ type clusters, although energetically higher than $MoPt_2$ type. Using a perturbative approach, namely the concentration wave analysis, Woodgate et al.[46] suggest that Cr and Co arrange in an $L1_0$ structure while Ni remains disordered. Numerous experimental investigations have also aimed to decipher possible ordering. Zhou *et al.* present experimental evidence for SRO from electron diffraction as well as atomic-resolution chemical mapping, involving Cr-enriched $\{\bar{3}11\}$ planes alternated with those enriched in Co and/or Ni[30]. However, the correlation between the indicating diffuse intensities and SRO was later questioned by Li *et al.*[47], who suggested that film effects rather than SRO influenced the observed diffraction patterns. Based on a data-driven electron-diffraction approach, Hsiao *et al.*[33] suggest that both $L1_2$ and $L1_1$ type of SRO, may occur depending on the actual sample preparation. However, Walsh *et al.*[48] suggests revisiting the connection between the diffraction pattern suggested for $L1_1$ ordering to other possible factors also. By atom probe tomography (APT) analysis, Inoue *et al.*[28] suggested that Cr-rich {001} atomic layers and (Ni+Co)-rich {001} layers tend to align mutually which would be consistent to a $L1_2$ ordering.

The discrepancies between different experimental and theoretical findings and the driving factor behind the SRO patterns remain therefore unclear. It has been sug-

* s.ghosh@mpie.de

gested that magnetism plays an important role in the phase stability of CrCoNi[49, 50] and may also impact the ordering tendencies. Several studies suggest an intrinsic interplay between magnetism and chemical ordering for this alloy[24, 29, 51]. Walsh *et al.*[29] suggested that magnetism is driving the ordering tendency resulting in a preferable alignment of antiferromagnetic Cr-Cr, Co-Cr nearest neighbor atom pairs, and ferromagnetic Co-Co atom pairs which would corroborate an $L1_2$ type of ordering. They also showed that the energy of the $L1_2$ type ordered structures is strongly affected by the magnetic alignment between the constituent atoms. On the other hand, the $MoPt_2$ type ordering, suggested in some theoretical studies as mentioned earlier, is not found to be much impacted by magnetism[31].

Therefore, the role of magnetism for the ordering tendencies in this alloy remains unclear. The main aim of the present work is, therefore, to utilize atomistic simulations to resolve the remaining ambiguities related to magnetism.

II. METHOD AND COMPUTATIONAL DETAILS

In the present work, density-functional theory (DFT) (details in Sec. II B) is used to compute the total energies for constructing efficient interatomic potentials which are introduced in Sec. II A. These potentials are used in subsequent Monte Carlo simulations (see Sec. II C) to investigate order-disorder phase transitions in the system. For selected configurations local magnetic interactions are computed using a complementary DFT approach outlined in Sec. II D and bonding analysis is carried out by studying crystal orbital Hamilton populations (COHP) based on band energy partitioning, as outlined in Sec. II E.

A. Low rank potentials (LRP)

We employ the low-rank interatomic potentials (LRP)[52, 53] as an interaction model in canonical Monte Carlo (MC) simulations. For this purpose, the total energy, E, for a given atomic configuration, σ, is defined as the sum of the individual contributions of local environments as

$$E(\sigma) = \sum_{\xi \in \Omega} V(\sigma(\xi + r_1), ..., \sigma(\xi + r_n)), \tag{1}$$

where Ω contains all lattice sites periodically repeated in space, V is the interatomic potential model in the tensor form, as described in Refs.[6, 52–54], ξ is the position of a central atom, $\sigma(\xi + r_i)$ is the species of the ith site and r_i is the vector connecting the central site with the ith neighbor, and n is the number of nearest neighbors in the environment, including the central atom ($n = 13$ in the present FCC case). Local lattice distortions can be incorporated as long as the topology of the supercell remains the same, i.e., each atom can be uniquely correlated with a given FCC lattice site. Further details on constructing and optimizing the LRP potentials can be found in Ref. [31, 54].

The dependence of V on its parameters is not linear. Thus, different local energy minima exist in the parameter space. Therefore, the minimization algorithm can find different local minima depending on the initial parameters. Different fits of LRPs provide hence independent energy predictions, and with a trained ensemble of several LRPs, the uncertainty level of the LRP model can be estimated.

The workflow is as outlined in Refs. [6, 31, 54]. At first, a training set and validation set containing DFT energies are prepared. Then an ensemble of 10 LRPs is trained, and their accuracy is checked with the validation dataset. With these LRPs, Monte Carlo simulations are carried out, and values of the specific heat capacity for the LRP ensemble are compared for different temperatures. To improve the accuracy of the LRPs, if needed, configurations corresponding to the temperature regime with larger deviations among the potentials in specific heat capacity are sampled and added to the training and validation set, and a new ensemble of 10 LRPs is trained. This procedure is continued until deviations in the predictions for the specific heat capacity calculated through different LRPs are reduced noticeably as discussed further below in Sec. III. With the trained ensemble of LRPs, we proceed with MC simulations on larger supercells than for the training dataset.

B. Density-functional theory calculations

The configurations in the training sets are calculated with spin-polarized density functional theory (DFT) as implemented in the Vienna Ab initio Simulation Package (VASP) 5.3.5[55–57] in combination with the projector augmented wave (PAW) method[58] and utilizing the Perdew-Burke-Ernzerhof generalized gradient approximation (PBE-GGA)[59] for the exchange-correlation functional. A fixed lattice parameter of 3.55 Å is used, which is in between the T=0 K theoretical and room temperature experimental lattice constants for CrCoNi[23, 25, 37, 60]. For the considered $3 \times 3 \times 3$ (108 atoms) supercell, an energy cut off of 300 eV and a Monkhorst-Pack $4 \times 4 \times 4$ k-mesh was used for the self-consistent calculations. Ionic relaxations of atomic positions with a fixed cell volume and shape are included in the calculations. The convergence criteria for the total energies and the forces on individual atoms are set to 10^{-3} eV and 10^{-2} eV/Å, respectively. A smearing parameter of 0.1 eV is used for the Fermi smearing. To include magnetism, each of the atomic configurations has been initialized with different random arrangements of magnetic spins, as will be discussed further below.

C. Monte Carlo simulations

The MC simulations are performed with periodic boundary conditions. We mainly focus on the temperature range of 50 – 2000 K. The simulations are carried out for systems with 108 and 864 atoms, i.e., $3\times3\times3$ and $6\times6\times6$ lattice units, based on a four-atom primitive FCC cell. The number of MC steps is 2×10^5 times the number of atoms in the corresponding supercell. To achieve an unbiased averaging, the so-called burn-in approach[61] is utilized, i.e., for each temperature, the first half of MC steps was neglected. The atomic structures were visualized with the VESTA software package[62].

D. Magnetic exchange interactions

The magnetic pair exchange parameters are computed to understand the nature of the magnetic interactions between constituent atom pairs present in the alloy. They are efficiently calculated using the multiple-scattering Green's function formalism as implemented in the SPRKKR code[63]. In this approach, the spin part of the Hamiltonian is mapped to a Heisenberg model:

$$H_{\text{Heisenberg}} = -\sum_{i\neq j} J_{ij}\mathbf{e}_i.\mathbf{e}_j, \tag{2}$$

where i, j represent atomic positions, and $\mathbf{e}_i$ denotes the unit vector along the direction of the magnetic moment at site i. The magnetic exchange interactions, J_{ij}, are computed using a perturbation approach [64] from energy differences due to small reorientations of spin pairs. Positive (negative) values for J_{ij} indicate ferromagnetic (antiferromagnetic) coupling between atoms i and j. For the actual SPRKKR calculations, an angular momentum cutoff of $l_{max} = 3$ and 56 complex energy points for the Green's functions integration are used. The energy convergence criterion was set to 10^{-6} eV for the self-consistent cycle.

E. Bonding analysis

To analyze the chemical bonds, the crystal orbital Hamilton populations (COHP)[65] are calculated using

$$\text{COHP}(E) = H_{\mu\nu}\sum_{j,\mathbf{k}} C^*_{\mu j}(\mathbf{k})C_{\nu j}(\mathbf{k})f_j\delta(\epsilon_j(\mathbf{k}) - E)w(\mathbf{k}), \tag{3}$$

where $C_{\mu j}$ is the coefficient of atomic orbital μ contributing to band j in the Linear Combination of Atomic Orbitals-Crystal Orbital (LCAO-CO) approach, and f_j is the occupation of band j. $H_{\mu\nu}$ corresponds to the Hamilton integral of atomic orbitals μ and ν. The COHP can be roughly understood as the density of states (DOS) weighted by covalent bonding energies. Previous studies have shown that the COHP of the hypothetical, non-spin-polarized model can serve as a semi-quantitative fingerprint for ferromagnetic and antiferromagnetic interactions [66, 67] in a system.

Spin-polarized and non-spin-polarized, static DFT calculations are performed with VASP 5.4.4 using the tetrahedron method with Blöchl's correction. The convergence criterion of the electronic structure is set to 10^{-6} eV, and the density of states is evaluated on 10,000 grid points. Projections onto a local basis and bonding analyses are performed with the program LOBSTER[65, 68–71] using the pbeVaspFit2015 basis set. The LOBSTER output is summarized and analyzed further with the LOBSTERPY package [72]. The COHP curves are visualized using the PYMATGEN package [73].

III. RESULTS AND DISCUSSION

In contrast to a non-magnetic alloy, for CrCoNi the total energy $E(\sigma)^m$ of each chemical configuration σ is not a unique number but can depend on the actual magnetic configuration m. This can, in principle, imply large energy differences for a given atomic configuration σ depending on how the local magnetic moments are initialized and converge to, as pointed out, e.g., by Walsh *et al.*[29]. Since the interatomic potentials, as given in Eq. 1, cannot account for energy differences caused by different magnetic states, fitting errors can be very large depending on the treatment of magnetism, as will be discussed later.

We therefore propose two treatments to overcome this problem, as sketched in Fig. 1. In the first approach, denoted as "magnetic relaxed", we probe for each chemical configuration σ the lowest magnetic energy. This corresponds to a situation at low temperatures or to a scenario where strong local magnetic order persists at ambient temperature. Magnetic short-range order can persist even at high temperatures if strong magnetic pair interactions exist. We will discuss later that, indeed, for some chemical configurations, strong local magnetic pair interactions are found, supporting this scenario. In the second approach, denoted as "magnetic disordered" in the following, each chemical configuration σ is assigned an energy $E(\sigma) = \langle E(\sigma)^m\rangle_m$ averaged over different magnetic configurations m, as in Ref. [31]. This corresponds to a high-temperature scenario for the paramagnetic state in analogy to the disordered-local moment approach. This can be motivated by the experimentally reported very low Curie temperature of around 4 K in CrCoNi alloy [74, 75]. However, in principle, the SRO could also be affected by magnetic entropy not accounted for in Ref. [31]. We will later discuss the impact of adding magnetic entropy to this approach in Sec. III D.

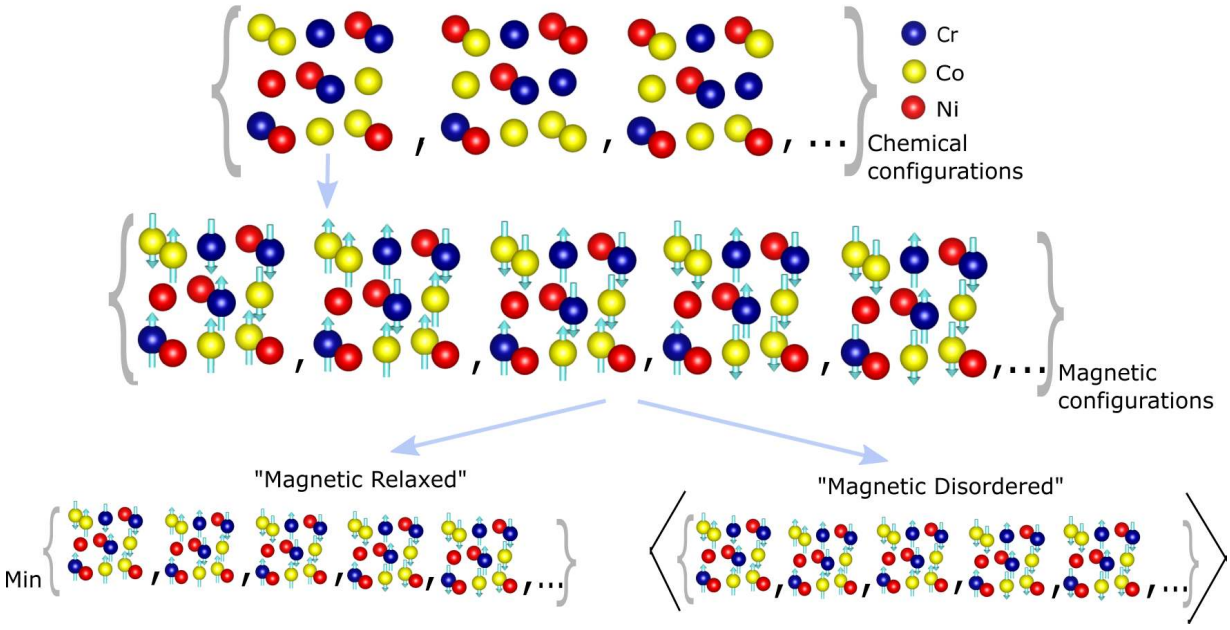

FIG. 1. Sketch of the two approaches used in the present work for treating magnetism. For each chemical configuration in the dataset, various magnetic states are computed. Two separate sets of potentials are trained; on the lowest magnetic state for each corresponding chemical configuration in the training set, denoted as "magnetic relaxed" and on the averaged magnetic energies, denoted as "magnetic disordered".

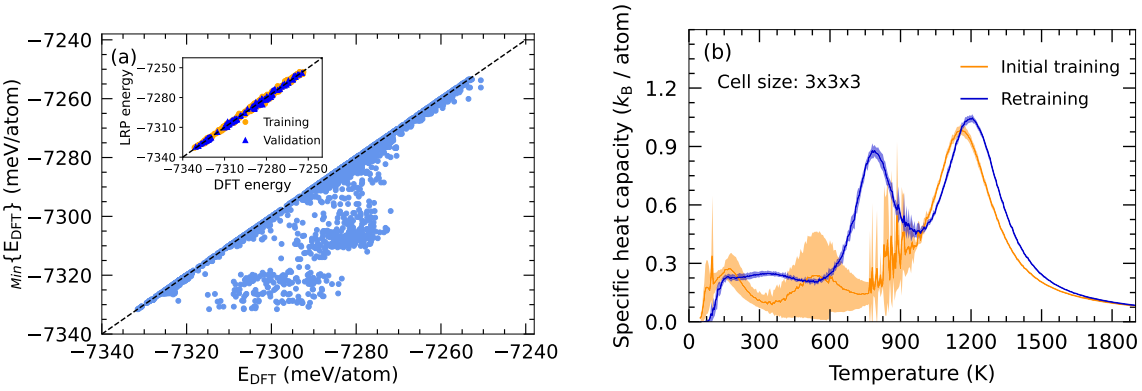

FIG. 2. (a) Energies of different magnetic snapshots against the lowest energy one for all chemical configurations in the dataset. The inset shows energy correlation for the "magnetic relaxed" scenario. (b) The temperature-dependent specific-heat capacity based on Monte Carlo simulation for equiatomic FCC CrCoNi alloy with a supercell size $3 \times 3 \times 3$ (i.e., 108 atoms) employing initially trained and retrained ensemble of 10 LRP potentials for the "magnetic relaxed" scenario.

A. The "magnetic relaxed" case

We first start with the "magnetic relaxed" case. We consider an initial DFT dataset of 345 chemical configurations, which includes random and $MoPt_2$ type ordered configurations, as used in Ref. [31]. In addition, we include a few $L1_2$ like ordered configurations where Cr atoms mainly occupy the FCC corner sites. For each chemical configuration σ, we initialized five different magnetic configurations m with different random arrangements of magnetic spins. In agreement with Walsh *et al.* observation [29], a large fluctuation in magnetic energies is observed for the $L1_2$ type ordered configurations for different m. This is shown in Fig. 2(a). Here the individual energies $E(\sigma)^m$ are plotted against their ground state minimum $_{\min}\{E(\sigma)^m\}$ values. Clearly, there are various $E(\sigma)^m$ showing significantly larger energies as compared to their minimum $_{\min}\{E(\sigma)^m\}$. To validate their impact on ordering, we train an ensemble of LRP potentials on only the lowest magnetic energy for each corresponding chemical configuration. We included 275 configurations in the training set and validated on 70 separate configurations. The mean validation error of these initially trained LRPs was around 1.4 meV/atom as av-

eraged over 10 LRPs with a standard deviation of 0.035 meV/atom. Apparently, if the potentials are trained on all different magnetic configurations, the fitting error for individual chemical configurations is as large as the energy fluctuations due to different magnetic states. Using the trained potentials, we performed MC simulations and analyzed the dependency of the specific heat capacity on temperature as shown in Fig. 2(b). The same lattice cell size of 3×3×3 (i.e., 108 atoms) was considered in the MC simulations as used for the actual DFT calculations entering the training set. These initially fitted potentials reveal at least two phase transitions which will be discussed below. As can be seen in Fig. 2(b), for the initially fitted potentials, significant fluctuations were observed among the ten different LRP potentials. For the retraining process, we sampled several new configurations within the range of temperatures 50 K to 1450 K with an interval of 40 K, including the regime near the observed phase transitions. As a result, 370 new chemical configurations were considered from MC simulations. In the retraining round we again considered five different initial magnetic configurations for each sampled chemical configuration and always selected the energetically most favorable magnetic state. The final training and validation sets included 570 and 145 configurations, respectively. The mean prediction error of the retrained LRPs was reduced to 1.25 meV/atom. The correlation plot between the DFT calculated and LRP predicted energies are shown in the inset of Fig. 2(a), revealing excellent agreement. The subsequent MC simulations employing the retrained potentials showed reduced fluctuations in the specific heat curves with a clear appearance of two phase transitions at about 1200 K and 800 K, as shown in Fig. 2(b).

To evaluate possible finite-size effects due to the chosen supercell size in the MC simulations, we performed simulations with a larger simulation cell of cell size 6×6×6 (i.e., containing 864 atoms). The temperature-dependent specific heat capacity is presented in Fig. 3(a). Compared with the "magnetic disordered" case of Ref. [31], we observe a high-temperature transition at around 1200 K, i.e., about 250 K above the previously reported one. Also, the nature of the phase transition changed, as can be observed from the variation of internal energies as a function of temperature, as shown in Fig. 3(b). In contrast to the first-order nature of the disordered to $MoPt_2$-type transition in Ref. [31], the transition is continuous. Moreover, as a consequence of probing the lowest magnetic energies, the ground state energies are also lower in the "magnetic relaxed" scenario. We further analyzed the chemical ordering through evaluated MC snapshots at various temperatures shown in Fig. 3(c). During the first transition at around 1200 K, the disordered alloy partially transforms to $L1_2/L1_0$-like ordering, i.e., $Cu_3Au/CuAu$-type structures with Cr occupying the Au sites and Co/Ni occupying the Cu sites (see structure at 1125 K). While cooling down, a second transition occurs at around 850 K driven by the separation of Co and Ni, forming Co-rich $L1_2$ and Ni-rich $L1_0$-type ordering with Cr. At very low temperatures, Co and Ni are fully separated. At 50 K we observe a phase separated $L1_2/L1_0$ type ordering which we denote as $(CrCo_3)_{L1_2}$+$(CrNi)_{L1_0}$ in the following.

As discussed in Ref. [31], the $MoPt_2$ like ordered structure is hardly affected by magnetism, whereas large energy fluctuations are observed for different magnetic states for these $L1_2/L1_0$ type ordering. To further evaluate this, we analyze in the following the microscopic magnetic interactions.

B. Magnetic interactions for $L1_2/L1_0$ configurations

To evaluate the microscopic origin of the underlying strong magnetic fluctuations, we first inspect the magnetic exchange interactions between different atom pairs in the observed low-temperature phase separated $(CrCo_3)_{L1_2}$ and $(CrNi)_{L1_0}$ phases. The results are presented in Fig. 4(a) and (b), respectively. The magnetic configurations and atomic cells are sketched in the insets. For $(CrCo_3)_{L1_2}$ shown in Fig. 4(a), where no Cr-Cr nearest-neighbor pairs are present in the first coordination shell, a comparable strong anti-ferromagnetic (negative) interaction between Co-Cr atom pairs is observed. This antiferromagnetic coupling trend between nearest neighbor Co-Cr is consistent with the findings of Walsh *et al.* in [29]. A modest Co-Co ferromagnetic pair interaction is found, which is about one-third of the value in pure Co[76].

The situation is qualitatively different for the $(CrNi)_{L1_0}$ structure (inset in Fig. 4(b)). In this case, Cr occupies, in addition to the corner sites (denoted as Cr1), partially the face-centered sites (denoted as Cr2). The nearest-neighbor interaction between two Cr atoms (denoted as Cr1-Cr2) in the first coordination shell is extremely large with a value of −29 meV. To provide context for this value, it is worth mentioning that the ferromagnetic nearest-neighbor exchange interaction in pure FCC Co, which is the element exhibiting the highest Curie temperature (1423 K), measures approximately 15 meV[76]. The here observed anti-ferromagnetic interaction of Cr atom pairs is about twice that large. These anti-ferromagnetic aligned Cr-Cr atom pairs in $L1_0$ type ordering play an important role in the magnetically driven stabilization of $L1_2/L1_0$ type ordering for the alloy. They also explain the large fluctuation in magnetic energies for these configurations. We note that recently also strong anti-ferromagnetic interactions between nearest-neighbor Cr atoms in the first coordination shell have been reported for ordered FCC $CrNi_2$ [77] alloys.

Similar findings are also observed for the $L1_2/L1_0$ like ordering found at higher temperatures above 800 K. We found that the strong anti-ferromagnetic interaction between nearest neighbor Cr atoms still exists for

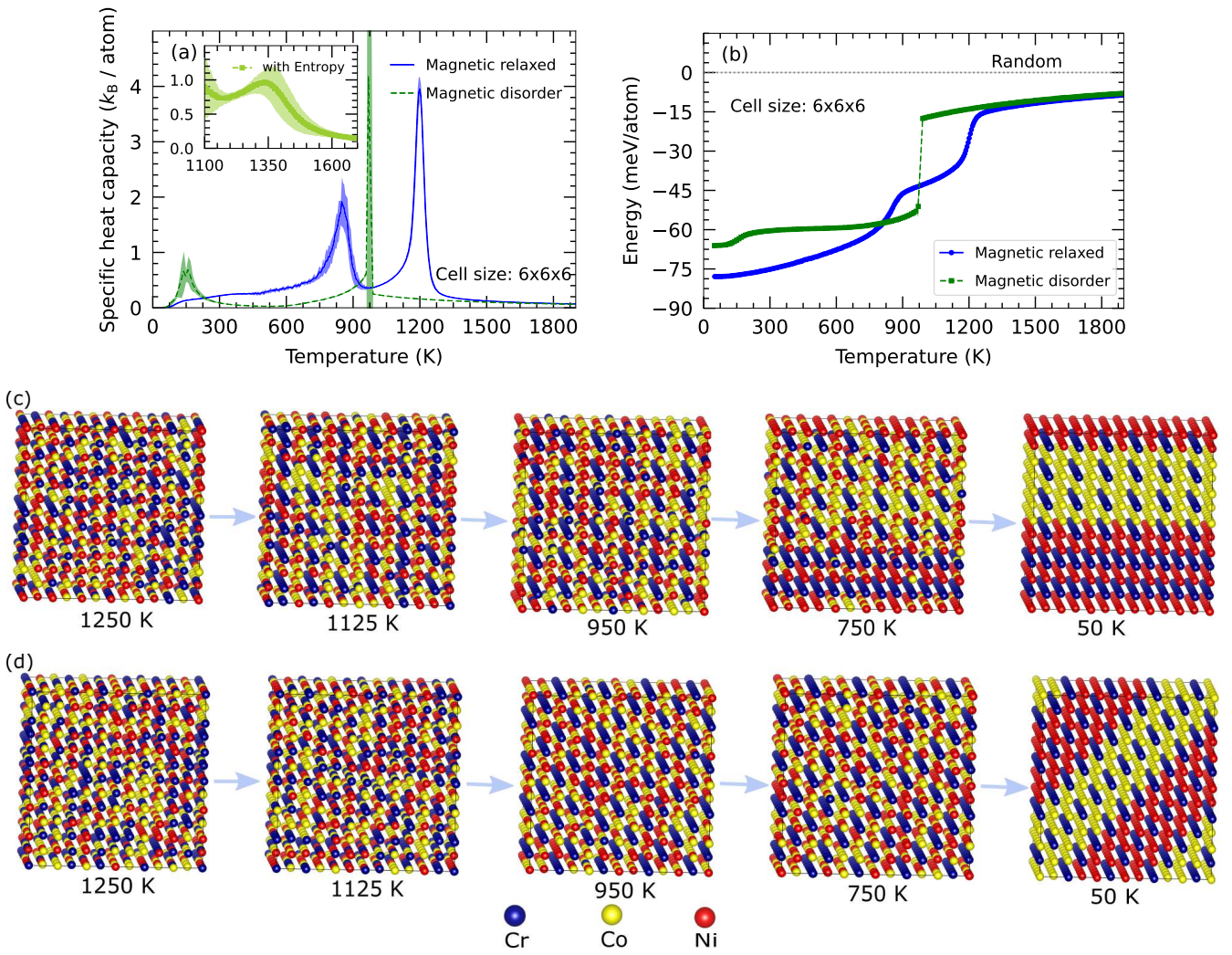

FIG. 3. (a) Temperature dependence of specific heat capacities for "magnetic relaxed" (blue) and "magnetic disordered" (green) cases obtained from MC simulations with supercell size: $6 \times 6 \times 6$ (i.e., 864 atoms). The specific heat capacity for the case including magnetic entropy to the "magnetic disordered" scenario is shown as inset (see Sec. III D for details). (b) The temperature dependence of mean internal energies from MC simulations for the "magnetic relaxed" (blue) and "magnetic disordered" (green) scenario. Atomic configurations at various temperatures extracted from MC snapshots are shown for the (c) "magnetic relaxed" and (d) "magnetic disordered" cases.

this ordering at higher temperatures (see details in appendix A).

As discussed in Ref. [31], only little impact of magnetism has been observed for the $MoPt_2$ type ordering in this alloy. We have done a similar analysis on the magnetic interactions for the $MoPt_2$ type $Cr(Co,Ni)_2$ structure too (with Co, Ni mixed on the Pt-sites) and observed only very weak magnetic interactions, (below ∼2 meV, see appendix A). That is why only a negligible impact of magnetism is observed for this type of ordering.

In order to further analyze the origin of the significant magnetic interactions in the low-temperature $(CrCo_3)_{L1_2}$ and $(CrNi)_{L1_0}$ phases, we performed a bonding analysis which will be discussed in the following.

C. Covalent bonding analysis for $L1_2/L1_0$ type configurations

We have performed a bonding analysis based on the COHP, which can be understood as a hopping-weighted density of states [65]. Its integration up to the Fermi level allows to estimate the covalent bond strength. We concentrate on the strongest nearest-neighbor Co–Co ferromagnetic interaction pairs in the $(CrCo_3)_{L1_2}$ phase and Cr–Cr anti-ferromagnetic interaction pairs in the $(CrNi)_{L1_0}$ phase (see Fig. 4). Further, to analyze the impact of magnetism on the COHP, we also performed a set of non-spin polarized calculations in addition to the spin-polarized calculations. In the following, the bonding (negative) contributions for the COHPs are plotted

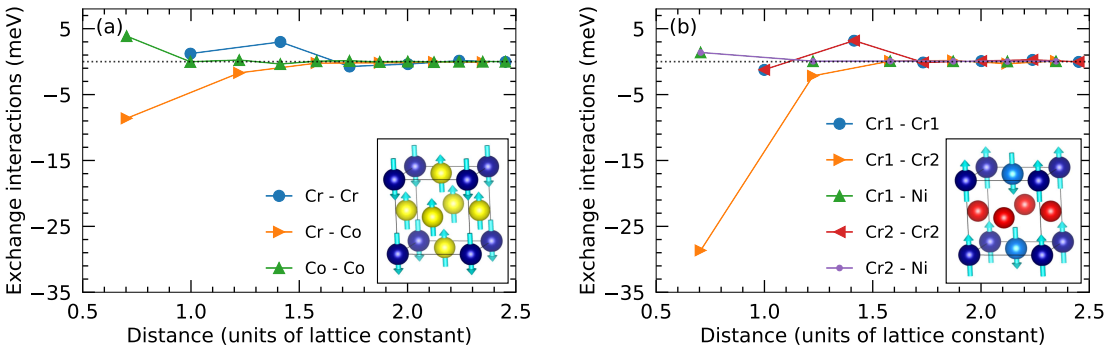

FIG. 4. Magnetic exchange interactions for different atom pairs as a function of distance (in units of lattice constant) between the pair of atoms in (a) $(CrCo_3)_{L1_2}$ and (b) $(CrNi)_{L1_0}$ phases, present in $(CrCo_3)_{L1_2}$+$(CrNi)_{L1_0}$ ordered structure obtained in "magnetic relaxed" scenario. Sketches of corresponding atomic and magnetic configurations are shown in insets.

to the right and anti-bonding (positive) contributions to the left.

In Fig. 5(a), inspecting the COHP for nearest neighbor Co–Co interaction in $(CrCo_3)_{L1_2}$ in the non-spin-polarized case, strong anti-bonding interactions at the Fermi level are revealed, indicating an electronic instability typical for ferromagnetic interactions [66]. Upon spin-polarization (see Fig. 5(b)), the COHPs of the spin-up and spin-down channels shift against each other in energy, similar to the results observed for transition metals prone to bandferromagnetism [66]. In this specific example, however, also the shape of the COHP curves changes (comparing Fig. 5(a) and (b)). The Co–Co bonds show an integrated COHP (ICOHP) value of −0.46 eV in the spin-polarized case. This value is comparable to nearest-neighbor interactions computed for FCC Co (−0.52 eV).

In the case of $(CrNi)_{L1_0}$, the non-spin-polarized nearest-neighbor Cr–Cr COHP (as shown in Fig. 5(c)) exhibits non-bonding states at the Fermi level and is not altered significantly upon spin polarization (see Fig. 5(d)). This is qualitatively different from the above-discussed ferromagnetic Co–Co interaction. It is, however, in agreement with the COHP-based magnetism theory of Landrum and Dronskowski in Ref. [66]. Similar to elemental Cr [67], the onset of anti-ferromagnetism is paralleled by a small decrease in the covalent bond strength of 0.07 eV. In addition, the integrated COHP of −1.20 eV for this bond in the spin-polarized case indicates a comparatively strong covalent interaction, similar to the bond strength computed for BCC Cr with a value of −1.16 eV. This strong covalent interaction, since measured by the integral over the hopping-weighted DOS, correlates with the strong magnetic interaction observed for Cr-Cr in $(CrNi)_{L1_0}$ (see Fig. 4(b)), indicating its microscopic origin.

D. "Magnetic disordered" case with and without magnetic entropy

In Ref. [31], the "magnetic disordered" approach has been applied, where the above-discussed $MoPt_2$ type of ordering has been observed. First, we verified that the same results were obtained if the $L1_2/L1_0$ found for the "magnetic relaxed" case were added manually to the training set. For this purpose, we considered the same dataset, but instead of using only the lowest magnetic energy, we averaged the magnetic energies over five different magnetic configurations for each chemical configuration to train the potentials. This set of fitted potentials also showed negligible fluctuations among the MC-simulated specific heat curves for the ten different LRP potentials. The chemical orderings through evaluated MC snapshots at various temperatures are shown in Fig. 3(d). The $MoPt_2$ type $Cr(Co,Ni)_2$ ordering is still obtained below the sharp transition at around 975 K in the "magnetic disordered" approach (green curves in Fig. 3(a) and (b)), as in Ref. [31]. We note that at a low temperature regime below 150 K a layered ordering is found, which is further discussed in the appendix B.

A fundamental approximation for the "magnetic disordered" case as performed in Ref. [31] has been, that only the mean magnetic energies entered, i.e., $\langle E(\sigma)^m \rangle_m$, but not the magnetic entropy S_{mag}. In a first approximation, the magnetic entropy can be estimated from the magnitude of the local magnetic moments[78–80] as

$$S_{\mathrm{mag}} = k_B \sum_i c_i \ln(|\mu_i| + 1), \tag{4}$$

where μ_i and c_i denote the averaged local magnetic moments and concentration of the ith atom type i.e. Cr, Co, Ni. To approximate the magnetic entropy for a given atomic configuration σ, we first computed the mean local magnetic moments of each of the three elements by averaging over the different magnetic configurations m and over the same atom type. Based on the effective local averaged moments $|\mu_i|$, $S(\sigma)_{\mathrm{mag}}$ was calculated for

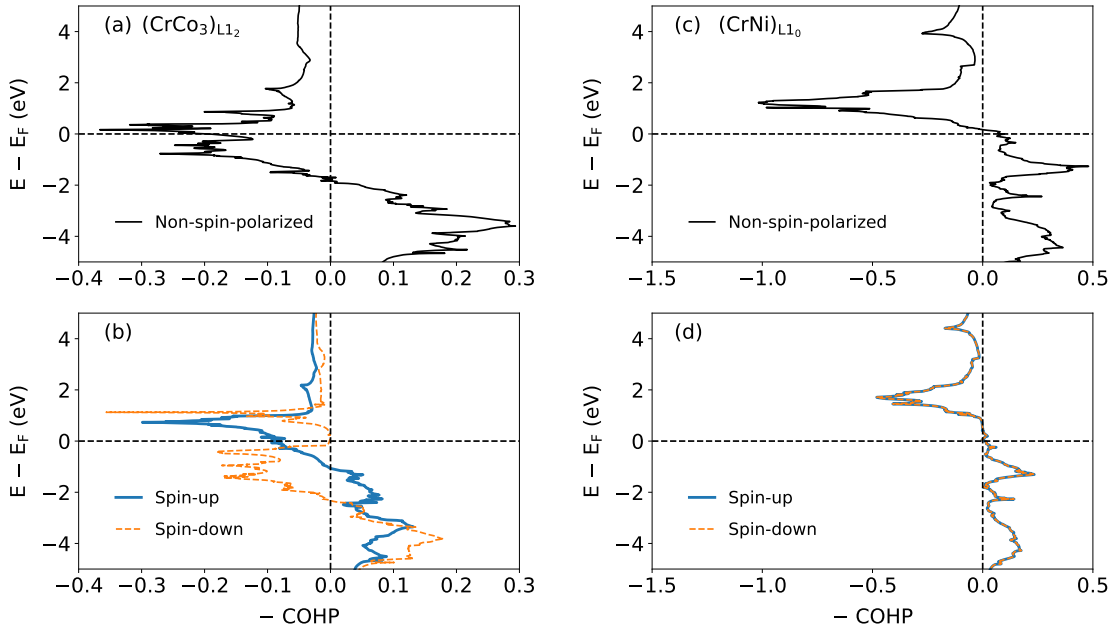

FIG. 5. COHP-based bonding analysis for [(a)-(b)] the strongest ferromagnetic Co–Co interaction in $(CrCo_3)_{L1_2}$ phase and [(c)-(d)] the strongest antiferromagnetic Cr–Cr interaction in $(CrNi)_{L1_0}$ phase for both non-spin-polarized and spin-polarized cases. The zero energy is set at Fermi energy (E_F).

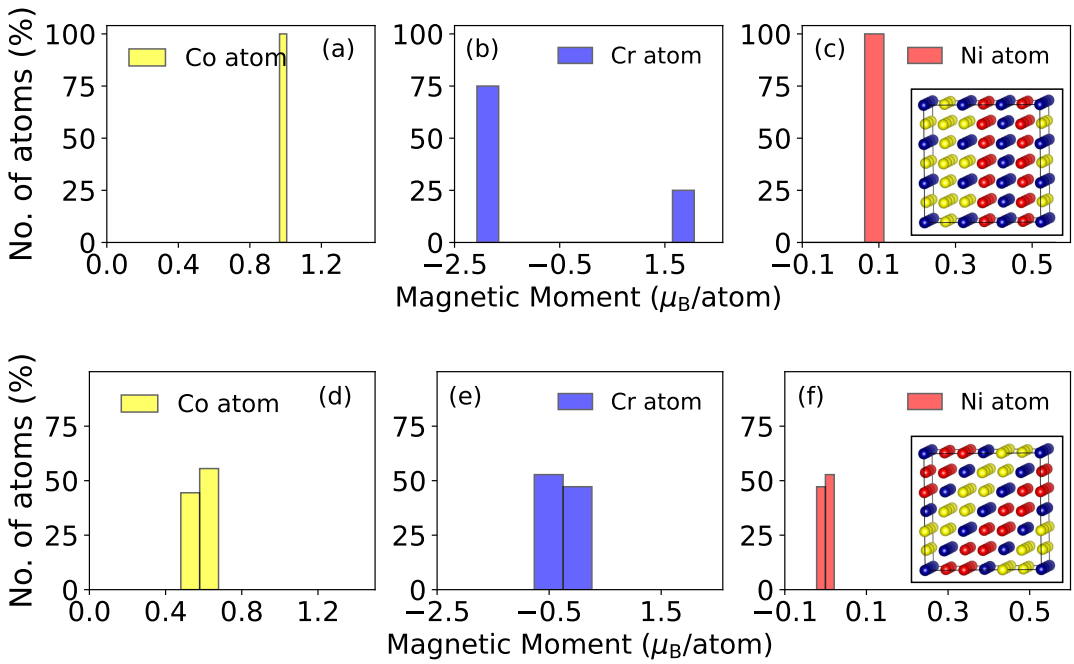

FIG. 6. Distribution of local magnetic moments for the three different atom types Co, Cr, and Ni corresponding to lowest energy magnetic states for structures obtained at 50 K from MC simulations in [(a)-(c)] "magnetic relaxed" and [(d)-(f)] "magnetic disordered" cases.

each chemical configuration σ according to Eq. 4. As the main ingredients are the local magnetic moments μ_i, we first evaluated the distribution of the local magnetic moments in the observed ordered configurations, i.e., $L1_2/L1_0$ (Fig. 6(a)-(c)) versus $MoPt_2$ type of ordering (Fig. 6(d)-(f)). In Fig. 6, the local moment distributions for the ordered structures at a low temperature of 50 K, as extracted from MC simulations, in "magnetic relaxed" and "magnetic disordered" scenarios are shown. The local moment distributions for the ordered configura-

tions at higher temperatures are qualitatively similar; see appendix C. When comparing the moment distributions (see Fig. 6) the most striking differences are observed for Co and Cr. For the $(CrCo_3)_{L1_2}$+$(CrNi)_{L1_0}$ structure, the average local magnetic moments for Co and Cr are found to be around 1 and 2 μ_B/atom whereas for the $MoPt_2$ structures, they are around 0.5 μ_B/atom. The Ni local magnetic moments are small in both cases. The global magnetic moment of both ordered configurations are about 0.02 μ_B/f.u. for the $L1_2/L1_0$-type structure and 0.11 μ_B/f.u. for the $MoPt_2$-type structure. Though both are very small, the smaller value in $L1_2/L1_0$-type structure is in slightly better agreement with the experimental observation[40, 81].

The significantly larger local magnetic moments for the $L1_2/L1_0$ type configurations indicate that these may have a larger magnetic entropy (see Eq. 4). This further motivates to investigate the role of magnetic entropy contributions in addition to the magnetic enthalpy entering the training sets. For that purpose, we calculated the magnetic entropy contribution at 1000 K according to Eq. 4 for each chemical configuration in the dataset and then added to the averaged magnetic enthalpy for the same, i.e., employing

$$F(\sigma) = \langle E(\sigma)^m \rangle_m - TS(\sigma)_{\mathrm{mag}}. \tag{5}$$

Thus every chemical configuration was assigned a free energy $F(\sigma)$, including the magnetic entropy contribution. Next, we trained a new set of 10 LRPs on these free energies and run subsequent Monte Carlo simulations to obtain the temperature-dependent specific heat capacities. Note that Eq. 4 overestimates the magnetic entropy due to its mean field nature, and our current choice of $T = 1000\ K$ in Eq. 4 limits its application to high temperatures. A computationally more expensive self-consistent approach applicable to arbitrary temperatures is beyond the scope of the present work and will be discussed elsewhere.

The results at high temperatures are shown as inset in Fig. 3(a). It can be seen that the inclusion of magnetic entropy contribution to the "magnetic disordered" case shifts the transition from 975 K to a higher temperature around 1350 K. Also, the transition is continuous in contrast to the first-order type of transition observed without taking S_{mag} into account. When analyzing the Monte Carlo obtained structures at around 1200 K below the transition including magnetic entropy, $L1_2/L1_0$ type of ordering tendency is observed accompanied by a tendency for Co-clustering. This contrasts the $MoPt_2$-type ordering found when magnetic entropy was not included. This again reveals the strong interlink between magnetism and the occurrence of the $L1_2/L1_0$ ordering.

IV. SUMMARY

We studied the interplay of chemical ordering and magnetism for FCC CrCoNi with two complementary magnetic treatments in combination with Monte Carlo simulations. In the first approach, magnetically favorable configurations have been selected, resulting in $L1_2/L1_0$-type of ordering. Analyzing the magnetic interactions, strong anti-ferromagnetic nearest-neighbor Cr–Cr interactions are found which contribute to the stabilization of these configurations also at elevated temperatures. A bonding analysis revealed that the strong magnetic interaction is microscopically rooted in the strong covalent interaction of Cr-Cr atom pairs in the $(CrNi)_{L1_0}$ phase. In contrast, if the magnetic degrees of freedom are averaged out, a $MoPt_2$ type of ordering is observed. This ordering, however, is suppressed in favor of $L1_2/L1_0$-type configurations as soon as magnetic entropy contributions are accounted for. These findings show the delicate interplay between magnetism and chemical interactions as well as subtle competition between the two types of ordered configurations. This subtle interplay is likely also the root of the discrepancies between the experimental findings suggesting $L1_2$ type ordering pattern[28, 33, 35] whereas several computational studies suggest $MoPt_2$ type ordering[31, 35, 45].

Our findings clearly show the possible implications of magnetism on chemical ordering, and, for cases where a full simultaneous sampling over both chemical and magnetic degrees of freedom is not feasible, the present approach of using two limiting scenarios provides a computationally straightforward solution.

ACKNOWLEDGEMENTS

S.G. and F.K. acknowledge the LRP and MC simulation packages by Alexander Shapeev and funding support from the Deutsche Forschungsgemeinschaft (DFG, 5080/3-1). J.G. would like to acknowledge the Gauss Centre for Super computing e.V. (www.gauss-centre.eu) for funding this project by providing computing time on the GCS Supercomputer SuperMUC-NG at Leibniz Super computing Centre (www.lrz.de) (project pn73da). We gratefully acknowledge fruitful discussions with Christopher Woodgate and Ashis Kundu.

Appendix A: Magnetic interactions in high temperature configurations of $L1_2/L1_0$ and $MoPt_2$ type orderings

As discussed in the main text, $(CrCo_3)_{L1_2}$ and $(CrNi)_{L1_0}$ phases at low temperatures, denoted as $(CrCo_3)_{L1_2}$+$(CrNi)_{L1_0}$ in the following, have shown significant magnetic interactions, in particular strong antiferromagnetic interactions between nearest-neighbor Cr

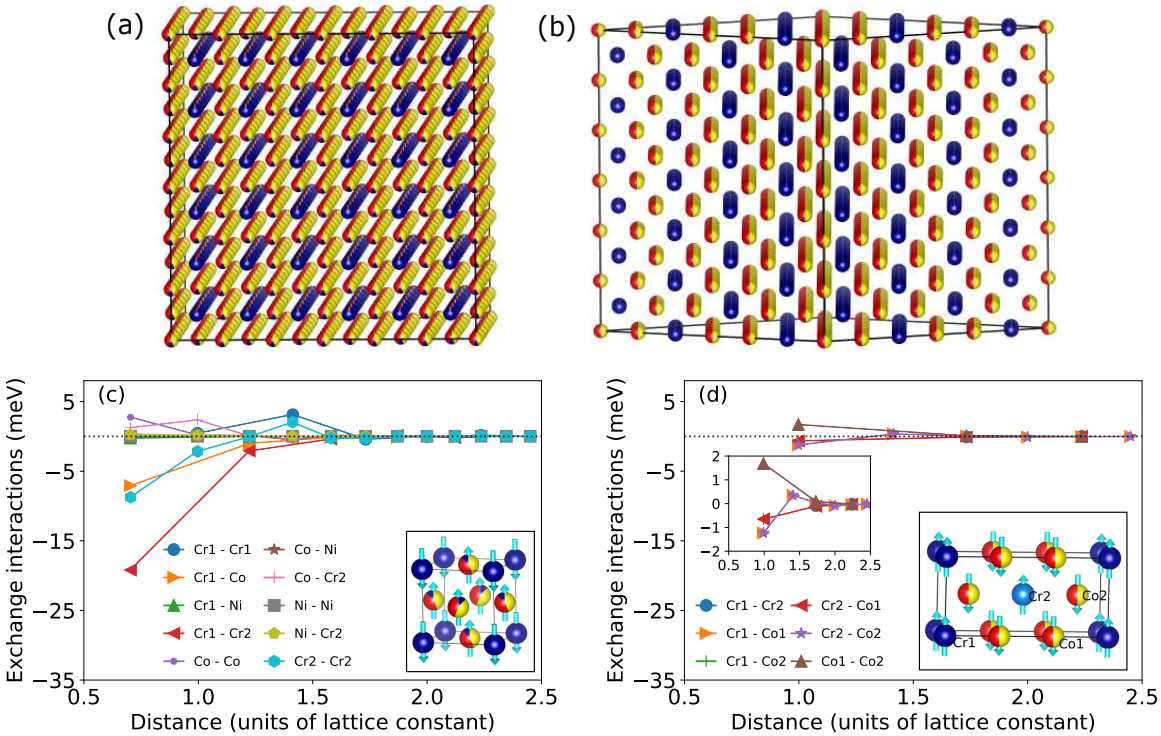

FIG. 7. Occupation probability of Cr, Co, Ni atoms on the lattice sites obtained from MC simulations at around 900 K in (a) "magnetic relaxed" and (b) "magnetic disordered" cases. Accordingly, magnetic exchange interactions are calculated for (c) $L1_2/L1_0$ type and (d) $MoPt_2$ type ordering. Insets: Sketches of the corresponding atomic and magnetic configurations.

atoms in $(CrNi)_{L1_0}$. Here we show that these strong interactions still persist in the single-phase ordered configuration as observed at higher temperatures (above 900 K, see Fig. 3(c)), as obtained in the "magnetic relaxed" scenario. In order to simplify the calculations we first deduct the effective site occupancy from the MC supercell simulations. As shown in Fig. 7(a), at higher temperatures, Cr atoms mainly occupy the corner sites of the FCC sublattice (denoted as Cr1) and the excess Cr (denoted as Cr2) as well as remaining Co and Ni atoms are occupying the face-centered sites. Based on this insight we performed magnetic exchange interaction calculations by constructing a four-atom FCC unit cell with 100% Cr on the corner sites (denoted as Cr1) and 12% Cr (denoted as Cr2), 44% Co and 44% Ni on the three face-centered sites (inset of Fig. 7(c)). The nearest-neighbor Cr1 and Cr2 atom pairs were initialized to be anti-ferromagnetically aligned to each other while Co spin moments were aligned parallel. This magnetic configuration is consistent with the ones observed from our supercell calculations. Inspecting the computed magnetic interactions, indeed a strong antiferromagnetic interaction between Cr1-Cr2 atom pairs is still present indicating that strong magnetic interactions are not suppressed by the sublattice disorder and can also persist at higher temperatures where the single-phase $L1_2/L1_0$ type ordering takes place.

We further investigated the magnetic interactions in the $MoPt_2$ type $Cr(Co,Ni)_2$ structure as obtained in the "magnetic disordered" case [31]. The occupation probability for the lattice sites as obtained from our Monte Carlo simulations is shown in Fig. 7(b). For the sake of simplicity we employed the orthorhombic representation of the $MoPt_2$-ordered cell as mentioned in Ref. [31] for computing the magnetic interactions. In contrast to the $L1_2/L1_0$ type ordering, much weaker magnetic interactions are observed. This is consistent with the marginal energy fluctuation for different magnetic scenarios for the $MoPt_2$ type chemical ordering.

We note that Walsh *et al.*[77] observed strong nearest neighbor Cr-Cr anti-ferromagnetic interactions in $MoPt_2$-ordered $CrNi_2$ alloy with preferred anti-ferromagnetic (AFM) chains of Cr atoms along [110] direction. We have also observed such AFM chains in our supercell calculations for $MoPt_2$-type ordered $Cr(Co,Ni)_2$ [31]. However, as also discussed above, in $MoPt_2$-ordered $Cr(Co,Ni)_2$, with mixed Co and Ni on the sublattice, no strong impact of magnetism has been found. In order to clarify the reasoning behind the difference between $Cr(Co,Ni)_2$ and $CrNi_2$ we first considered the phase-separated $MoPt_2$-ordered $CrCo_2$ and $CrNi_2$ structures. It is found that the AFM chain of Cr atoms along [110] direction is indeed the preferred magnetic configuration for $CrNi_2$, however for $CrCo_2$ structure, all Cr atoms prefer to align anti-parallel to the Co atoms leading to FM chains of Cr spin moments. When mixing Co and Ni on

the sublattice, i.e. considering $MoPt_2$-type $Cr(Co,Ni)_2$ ordering, the energy obtained for magnetic configurations is therefore robust with the magnetic alignments of the Cr atoms, with energy differences of less than 1.5 meV/atom. This indicates that in contrast to the binary $MoPt_2$-type $CrCo_2$ and $CrNi_2$ configurations, the magnetic alignment of the Cr-spins is suppressed for $Cr(Co,Ni)_2$. This observation also justifies our consideration of ferromagnetic alignment of nearest neighbor Cr atoms (i.e. Cr1-Cr1 atom pairs) for $Cr(Co,Ni)_2$ (see inset of Fig. 7(d)) when calculating the magnetic interaction parameters with the orthorhombic representation of $MoPt_2$ ordering, which, due to the inherent symmetry, only allows for ferromagnetic alignment.

Appendix B: Low temperature ordering for "magnetic disordered" scenario

In the "magnetic disordered" scenario, at low temperatures, below 150 K, a special layered ordering of $MoPt_2$ type appears (see inset of Fig. 6(f)), which is around 2.5 meV/atom lower in energy as compared to the phase separated $(CrCo_2+CrNi_2)_{MoPt_2}$ structure reported earlier in Ref. [31]. To put this into perspective, when relaxing the magnetic degree of freedom ("magnetic relaxed" scenario), the $L1_2/L1_0$ type $(CrCo_3)_{L1_2}+(CrNi)_{L1_0}$ structures are anyway lower in energy by about 11 meV/atom. Moreover, for a rigorous ground-state search, which is beyond the scope of the present work, also volume and shape relaxations, not included in the present study, may further alter the ordering. Keeping in mind in addition that these configurations are experimentally hardly accessible due to slow kinetics, we did not investigate this aspect further.

Appendix C: Magnetic distributions for higher temperature configurations

We evaluated the local moment distributions of Cr, Co, and Ni atoms in the ordered structures appearing around 900 K with different corresponding magnetic configurations for both "magnetic relaxed" and "magnetic disordered" cases, as shown in Fig. 8. We observe that, compared to the low-temperature ordered structures (see Fig. 6), the distributions are comparatively broad, but the trend of larger local moments in $L1_2/L1_0$ ordering (Fig. 8(a)-(c)) as compared to those found in the $MoPt_2$ type ordering (Fig. 8(d)-(f)) still persists which can give rise to larger magnetic entropy contributions for the $L1_2/L1_0$ type, as discussed in Sec. III D.

[1] D. King, S. Middleburgh, L. Edwards, G. Lumpkin, and M. Cortie, Jom **67**, 2375 (2015).
[2] M. Widom, W. P. Huhn, S. Maiti, and W. Steurer, Metallurgical and Materials Transactions A **45**, 196 (2014).
[3] S. Maiti and W. Steurer, Acta Materialia **106**, 87 (2016).
[4] Y. Wu and D. L. Irving, Applied Physics Letters **119**, 111901 (2021).
[5] S. Zhao, Journal of Phase Equilibria and Diffusion **42**, 578 (2021).
[6] T. Kostiuchenko, A. V. Ruban, J. Neugebauer, A. Shapeev, and F. Körmann, Physical Review Materials **4**, 113802 (2020).
[7] P. Singh, A. V. Smirnov, and D. D. Johnson, Physical Review B **91**, 224204 (2015).
[8] X. Chen, Q. Wang, Z. Cheng, M. Zhu, H. Zhou, P. Jiang, L. Zhou, Q. Xue, F. Yuan, J. Zhu, *et al.*, Nature **592**, 712 (2021).
[9] C. Niu, A. Zaddach, A. Oni, X. Sang, J. Hurt III, J. LeBeau, C. Koch, and D. Irving, Applied Physics Letters **106**, 161906 (2015).
[10] B. Schönfeld, C. R. Sax, J. Zemp, M. Engelke, P. Boesecke, T. Kresse, T. Boll, T. Al-Kassab, O. E. Peil, and A. V. Ruban, Physical Review B **99**, 014206 (2019).
[11] Y. Ma, Q. Wang, C. Li, L. J. Santodonato, M. Feygenson, C. Dong, and P. K. Liaw, Scripta Materialia **144**, 64 (2018).
[12] Q. Ding, Y. Zhang, X. Chen, X. Fu, D. Chen, S. Chen, L. Gu, F. Wei, H. Bei, Y. Gao, *et al.*, Nature **574**, 223 (2019).
[13] S. Mu, J. Yin, G. D. Samolyuk, S. Wimmer, Z. Pei, M. Eisenbach, S. Mankovsky, H. Ebert, and G. M. Stocks, Physical Review Materials **3**, 014411 (2019).
[14] Z. Rao, B. Dutta, F. Körmann, D. Ponge, L. Li, J. He, L. Stephenson, L. Schäfer, K. Skokov, O. Gutfleisch, *et al.*, Physical Review Materials **4**, 014402 (2020).
[15] Y. Zhang, Y. Zhuang, A. Hu, J.-J. Kai, and C. T. Liu, Scripta Materialia **130**, 96 (2017).
[16] Y. Ikeda, F. Körmann, I. Tanaka, and J. Neugebauer, Entropy **20**, 655 (2018).
[17] S. Zhao, Y. Osetsky, G. M. Stocks, and Y. Zhang, npj Computational Materials **5**, 1 (2019).
[18] Q.-J. Li, H. Sheng, and E. Ma, Nature communications **10**, 1 (2019).
[19] E. Antillon, C. Woodward, S. Rao, B. Akdim, and T. Parthasarathy, Acta Materialia **190**, 29 (2020).
[20] Y. Wu, F. Zhang, X. Yuan, H. Huang, X. Wen, Y. Wang, M. Zhang, H. Wu, X. Liu, H. Wang, *et al.*, Journal of Materials Science & Technology **62**, 214 (2021).
[21] X. Wu, Journal of Materials Science & Technology (2022).
[22] S. Yang, M. Jiang, H. Li, Y. Liu, and L. Wang, Rare Metals **31**, 75 (2012).
[23] A. Tamm, A. Aabloo, M. Klintenberg, M. Stocks, and A. Caro, Acta Materialia **99**, 307 (2015).
[24] F. Zhang, S. Zhao, K. Jin, H. Xue, G. Velisa, H. Bei, R. Huang, J. Ko, D. Pagan, J. Neuefeind, *et al.*, Physical review letters **118**, 205501 (2017).
[25] J. Ding, Q. Yu, M. Asta, and R. O. Ritchie, Proceedings of the National Academy of Sciences **115**, 8919 (2018).
[26] R. Zhang, S. Zhao, J. Ding, Y. Chong, T. Jia, C. Ophus, M. Asta, R. O. Ritchie, and A. M. Minor, Nature **581**, 283 (2020).

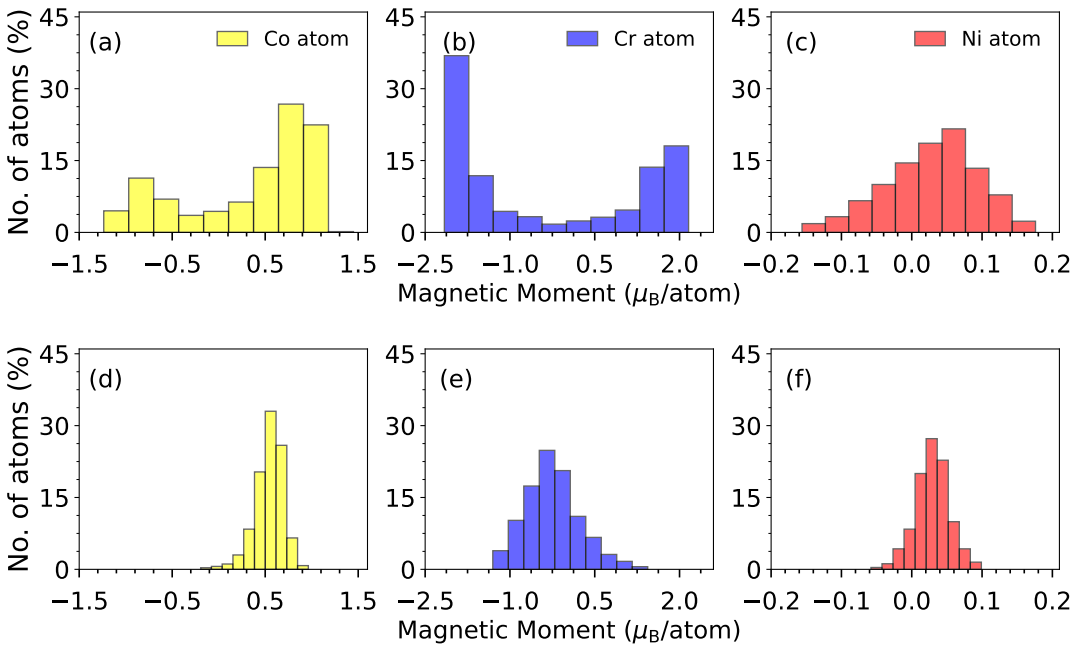

FIG. 8. Distribution of local magnetic moments for two types of exemplary configurations at around 910 K, [(a)-(c)] $L1_2/L1_0$ type (in "magnetic relaxed" case) and [(d)-(f)] $MoPt_2$ type (in "magnetic disordered" case) ordered structures.

[27] Z. Pei, R. Li, M. C. Gao, and G. M. Stocks, npj Computational Materials **6**, 1 (2020).
[28] K. Inoue, S. Yoshida, and N. Tsuji, Physical Review Materials **5**, 085007 (2021).
[29] F. Walsh, M. Asta, and R. O. Ritchie, Proceedings of the National Academy of Sciences **118** (2021).
[30] L. Zhou, Q. Wang, J. Wang, X. Chen, P. Jiang, H. Zhou, F. Yuan, X. Wu, Z. Cheng, and E. Ma, Acta Materialia **224**, 117490 (2022).
[31] S. Ghosh, V. Sotskov, A. V. Shapeev, J. Neugebauer, and F. Körmann, Physical Review Materials **6**, 113804 (2022).
[32] G. Tang, Z. Zhang, Y. Liu, Y. Wang, X. Wu, and X. Liu, Materials & Design **225**, 111572 (2023).
[33] H.-W. Hsiao, R. Feng, H. Ni, K. An, J. D. Poplawsky, P. K. Liaw, and J.-M. Zuo, Nature communications **13**, 6651 (2022).
[34] M. Zhang, Q. Yu, C. Frey, F. Walsh, M. I. Payne, P. Kumar, D. Liu, T. M. Pollock, M. D. Asta, R. O. Ritchie, *et al.*, Acta Materialia **241**, 118380 (2022).
[35] S. Picak, P. Singh, D. Salas, M. Tunes, X. Fang, L. Zhou, M. Kramer, Y. Chumlyakov, D. Johnson, R. Arroyave, *et al.*, Materials Science and Engineering: A , 145309 (2023).
[36] B. Gludovatz, A. Hohenwarter, K. V. Thurston, H. Bei, Z. Wu, E. P. George, and R. O. Ritchie, Nature communications **7**, 1 (2016).
[37] G. Laplanche, A. Kostka, C. Reinhart, J. Hunfeld, G. Eggeler, and E. George, Acta Materialia **128**, 292 (2017).
[38] C. Slone, S. Chakraborty, J. Miao, E. P. George, M. J. Mills, and S. Niezgoda, Acta Materialia **158**, 38 (2018).
[39] C. Slone, J. Miao, E. P. George, and M. J. Mills, Acta Materialia **165**, 496 (2019).
[40] B. C. Sales, K. Jin, H. Bei, G. M. Stocks, G. D. Samolyuk, A. F. May, and M. A. McGuire, Scientific reports **6**, 26179 (2016).
[41] D. Liu, Q. Yu, S. Kabra, M. Jiang, P. Forna-Kreutzer, R. Zhang, M. Payne, F. Walsh, B. Gludovatz, M. Asta, *et al.*, Science **378**, 978 (2022).
[42] S. Rideout, W. Manly, E. Kamen, B. Lement, and P. A. Beck, JoM **3**, 872 (1951).
[43] G. Zhmurko, E. Kabanova, V. Kuznetsov, and A. Leonov, Moscow University chemistry bulletin **63**, 234 (2008).
[44] T. Omori, J. Sato, K. Shinagawa, I. Ohnuma, K. Oikawa, R. Kainuma, and K. Ishida, Journal of phase equilibria and diffusion **35**, 178 (2014).
[45] J.-P. Du, P. Yu, S. Shinzato, F.-S. Meng, Y. Sato, Y. Li, Y. Fan, and S. Ogata, Acta Materialia **240**, 118314 (2022).
[46] C. D. Woodgate and J. B. Staunton, Physical Review B **105**, 115124 (2022).
[47] L. Li, Z. Chen, S. Kuroiwa, M. Ito, K. Yuge, K. Kishida, H. Tanimoto, Y. Yu, H. Inui, and E. P. George, Acta Materialia **243**, 118537 (2023).
[48] F. Walsh, M. Zhang, R. O. Ritchie, A. M. Minor, and M. Asta, Nature Materials **22**, 926 (2023).
[49] C. Niu, C. R. LaRosa, J. Miao, M. J. Mills, and M. Ghazisaeidi, Nature communications **9**, 1363 (2018).
[50] P. Papež, M. Zelený, M. Friák, and I. Dlouhý, Materials Chemistry and Physics **304**, 127783 (2023).
[51] C. D. Woodgate, D. Hedlund, L. Lewis, and J. B. Staunton, Physical Review Materials **7**, 053801 (2023).
[52] A. Shapeev, Computational Materials Science **139**, 26 (2017).
[53] E. A. Meshkov, I. I. Novoselov, A. V. Shapeev, and A. V. Yanilkin, Intermetallics **112**, 10.1016/j.intermet.2019.106542 (2019).

[54] T. Kostiuchenko, F. Körmann, J. Neugebauer, and A. Shapeev, npj Computational Materials **5**, 10.1038/s41524-019-0195-y (2019).

[55] G. Kresse and J. Hafner, Physical review B **47**, 558 (1993).

[56] G. Kresse and J. Hafner, Physical Review B **49**, 14251 (1994).

[57] G. Kresse and J. Furthmüller, Computational materials science **6**, 15 (1996).

[58] P. E. Blöchl, Physical review B **50**, 17953 (1994).

[59] J. P. Perdew, K. Burke, and M. Ernzerhof, Physical review letters **77**, 3865 (1996).

[60] S. S. Sohn, A. Kwiatkowski da Silva, Y. Ikeda, F. Körmann, W. Lu, W. S. Choi, B. Gault, D. Ponge, J. Neugebauer, and D. Raabe, Advanced Materials **31**, 1807142 (2019).

[61] M. K. Cowles and B. P. Carlin, Journal of the American Statistical Association **91**, 883 (1996).

[62] K. Momma and F. Izumi, Journal of applied crystallography **44**, 1272 (2011).

[63] H. Ebert, D. Koedderitzsch, and J. Minar, Reports on Progress in Physics **74**, 096501 (2011).

[64] A. I. Liechtenstein, M. Katsnelson, V. Antropov, and V. Gubanov, Journal of Magnetism and Magnetic Materials **67**, 65 (1987).

[65] R. Dronskowski and P. E. Bloechl, The Journal of Physical Chemistry **97**, 8617 (1993).

[66] G. A. Landrum and R. Dronskowski, Angewandte Chemie International Edition **39**, 1560 (2000).

[67] A. Decker, G. A. Landrum, and R. Dronskowski, Zeitschrift für anorganische und allgemeine Chemie **628**, 303 (2002).

[68] V. L. Deringer, A. L. Tchougréeff, and R. Dronskowski, The Journal of Physical Chemistry A **115**, 5461 (2011).

[69] S. Maintz, V. L. Deringer, A. L. Tchougréeff, and R. Dronskowski, Journal of Computational Chemistry **34**, 2557 (2013).

[70] S. Maintz, V. L. Deringer, A. L. Tchougréeff, and R. Dronskowski, Journal of computational chemistry **37**, 1030 (2016).

[71] R. Nelson, C. Ertural, J. George, V. L. Deringer, G. Hautier, and R. Dronskowski, Journal of computational chemistry **41**, 1931 (2020).

[72] J. George, G. Petretto, A. Naik, M. Esters, A. J. Jackson, R. Nelson, R. Dronskowski, G.-M. Rignanese, and G. Hautier, ChemPlusChem , e202200123 (2022).

[73] S. P. Ong, W. D. Richards, A. Jain, G. Hautier, M. Kocher, S. Cholia, D. Gunter, V. L. Chevrier, K. A. Persson, and G. Ceder, Computational Materials Science **68**, 314 (2013).

[74] K. Jin, B. C. Sales, G. M. Stocks, G. D. Samolyuk, M. Daene, W. J. Weber, Y. Zhang, and H. Bei, Scientific reports **6**, 1 (2016).

[75] D. Billington, A. D. James, E. I. Harris-Lee, D. A. Lagos, D. O'Neill, N. Tsuda, K. Toyoki, Y. Kotani, T. Nakamura, H. Bei, *et al.*, Physical Review B **102**, 174405 (2020).

[76] M. Pajda, J. Kudrnovskỳ, I. Turek, V. Drchal, and P. Bruno, Physical Review B **64**, 174402 (2001).

[77] F. Walsh, R. O. Ritchie, and M. Asta, Physical Review Materials **6**, 113602 (2022).

[78] G. Inden, in *Proc. Project Meeting CALPHAD* (Düsseldorf Inst. Duesseldorf, 1976) pp. 1–13.

[79] F. Körmann, A. A. H. Breidi, S. L. Dudarev, N. Dupin, G. Ghosh, T. Hickel, P. Korzhavyi, J. A. Munoz, and I. Ohnuma, physica status solidi (b) **251**, 53 (2014).

[80] D. Ma, B. Grabowski, F. Körmann, J. Neugebauer, and D. Raabe, Acta Materialia **100**, 90 (2015).

[81] F. Mustafa, M. Egilmez, W. Abuzaid, S. El-Khatib, T. Nawaz, S. Ahmad, and S. Alagoz, Materials **16**, 1044 (2023).